Unraveling the Hybrid Origins of the X-Ray Nonthermal Emission from IGR J17091-3624

N.B. When citing this work, cite the original published paper.

(article starts on next page)

CrossMark

Unraveling the Hybrid Origins of the X-Ray Nonthermal Emission from IGR J17091–3624

Zikun Lin[1,2] , Yanan Wang[1] , Santiago del Palacio[3] , Mariano Méndez[4] , Shuang-Nan Zhang[2,5] , Thomas D. Russell[6] , Long Ji[7] , Jin Zhang[8] , Liang Zhang[5] , Diego Altamirano[9] , and Jifeng Liu[1,2,10,11]

[1] Key Laboratory of Optical Astronomy, National Astronomical Observatories, Chinese Academy of Sciences, Beijing 100101, People's Republic of China; wangyn@bao.ac.cn
[2] School of Astronomy and Space Sciences, University of Chinese Academy of Sciences, Beijing 100049, People's Republic of China
[3] Department of Space, Earth and Environment, Chalmers University of Technology, SE-412 96 Gothenburg, Sweden
[4] Kapteyn Astronomical Institute, University of Groningen, PO Box 800, CH-9700 AV Groningen, The Netherlands
[5] Key Laboratory of Particle Astrophysics, Institute of High Energy Physics, Chinese Academy of Sciences, 19B Yuquan Road, Beijing 100049, People's Republic of China
[6] INAF, Istituto di Astrofisica Spaziale e Fisica Cosmica, via Ugo la Malfa 153, 90146 Palermo, Italy
[7] School of Physics and Astronomy, Sun Yat-sen University, Zhuhai 519082, People's Republic of China
[8] School of Physics, Beijing Institute of Technology, Beijing 100081, People's Republic of China
[9] School of Physics and Astronomy, University of Southampton, Southampton, Hampshire SO17 1BJ, UK
[10] Institute for Frontiers in Astronomy and Astrophysics, Beijing Normal University, Beijing 102206, People's Republic of China
[11] New Cornerstone Science Laboratory, National Astronomical Observatories, Chinese Academy of Sciences, Beijing 100012, People's Republic of China

Abstract

We present a comprehensive study based on multiwavelength observations from the NuSTAR, NICER, Swift, Fermi, NEOWISE, and ATCA telescopes during the 2022 outburst of the black-hole X-ray binary IGR J17091–3624. Our investigation concentrates on the heartbeat-like variability in the X-ray emission, with the aim of using it as a tool to unravel the origin of the nonthermal emission during the heartbeat state. Through X-ray timing and spectral analysis, we observe that the heartbeat-like variability correlates with changes in the disk temperature, supporting the disk radiation pressure instability scenario. Moreover, in addition to a Comptonization component, our time-averaged and phase-resolved spectroscopy reveal the presence of a power-law component that varies independently from the disk component. Combined with the radio–X-ray spectral energy distribution fitting, our results suggest that the power-law component could originate from synchrotron self-Compton radiation in the jet, which requires a strong magnetic field of about $B = (0.3–3.5) \times 10^6$ G. Additionally, assuming that IGR J17091-3624 and GRS 1915 + 105 share the same radio–X-ray correlation coefficient during both the hard and the heartbeat states, we obtain a distance of 13.7 ± 2.3 kpc for IGR J17091–3624.

Unified Astronomy Thesaurus concepts: Accretion (14); X-ray transient sources (1852); Black hole physics (159); Jets (870)

1. Introduction

Black-hole X-ray binaries (BHXRBs) are a type of celestial system that consist of a black hole in a close orbit, accreting material from its companion star, and show repeated outbursts with a cadence of years. During outbursts, the radiation of BHXRBs consists of thermal and/or nonthermal components. The thermal component is typically represented by a multicolor blackbody emission, emanating from the accretion disk in the soft X-ray band (see, e.g., Shakura & Sunyaev 1973). The nonthermal emissions in the X-ray band are particularly complex, primarily attributable to processes such as Comptonization and synchrotron radiation occurring in different regions, which make them enduring enigmas in high-energy astrophysics (see, e.g., Illarionov & Siuniaev 1975; Rybicki & Lightman 1979).

The nonthermal X-ray emission from BHXRBs has been generally believed to be dominated by a hot, optically thin electron gas cloud—commonly termed as the "corona"—which undergoes inverse Compton scattering with seed photons from the accretion disk, resulting in a (cutoff) power-law spectrum (see, e.g., Sunyaev & Titarchuk 1980; Haardt & Maraschi 1993; Gilfanov 2010; García et al. 2021, 2022). Photons reflecting back to the disk from the corona produce an iron Kα emission line, peaking at 6.4–6.9 keV, which is broadened by Doppler and relativistic effects along with a Compton hump peaking at around 10–30 keV (see, e.g., Lightman & Rybicki 1980; Lightman et al. 1981; Fabian et al. 1989; Dauser et al. 2010; García et al. 2014; Dauser et al. 2022). On the other hand, jets have been indicated to emit a broad spectrum ranging from radio to gamma rays through synchrotron and synchrotron self-Compton (SSC) radiation. The emission at high energies displays a power-law spectrum in the optically thin regime, represented as $F_\nu \propto \nu^\alpha$ (see, e.g., Marscher 1983; Sari et al. 1998; Sari & Esin 2001; Finke et al. 2008; Nakar & Piran 2011; Hoshino 2013; Ball et al. 2018). Despite numerous efforts, differentiating these emission regions between corona and jets using only X-ray data has been unsuccessful (e.g., Heinz 2004; Markoff et al. 2005). However, more recent approaches using varied techniques, i.e., well-defined optical/near-infrared jet emission and polarization measurement, have successfully demonstrated that nonthermal X-ray emission may sometimes originate from jets (e.g., Russell et al. 2010; Russell & Shahbaz 2014; Chattopadhyay et al. 2024). Furthermore,

broadband spectral energy distribution (SED) fitting has emerged as an effective method for distinguishing nonthermal emissions (e.g., Russell & Shahbaz 2014; Punsly 2011; Kantzas et al. 2021; Rodi et al. 2021).

Timing analysis, which involves studying the variability in the lightcurve across different energy bands, also aids in our understanding of the correlation between the disk, corona, and jet (e.g., Wang et al. 2021; Méndez et al. 2022). As the jet moves perpendicularly away from the accretion disk with relativistic speed (e.g., Pushkarev et al. 2009, 2017; Tetarenko et al. 2017; Miller-Jones et al. 2019; Zdziarski et al. 2022), the scattering efficiency between disk photons and jet electrons significantly decreases compared with the disk and corona (e.g., Wilkins & Fabian 2012). Long-term variability (lasting hours to days) between the disk and jet could remain correlated (e.g., Fender et al. 2004; Vincentelli et al. 2023; You et al. 2023), but short-term oscillations (lasting several seconds) originating from the disk are expected to dilute during the propagation (e.g., Eikenberry et al. 1998). Thus, integrating timing analysis of short-term variability from the disk with broadband SED spectroscopy could elucidate the radiation mechanisms in BHXRBs.

Heartbeat variability in BHXRBs, characterized by quasi-periodic flares in X-ray emission, is suggested to stem from the radiation pressure instability of the accretion disk (e.g., Janiuk et al. 2000; Nayakshin et al. 2000; Neilsen et al. 2011, 2012; Yan et al. 2017). Such a phenomenon is associated with a limit-cycle behavior in the accretion rate and disk surface density, resulting in a continuous evacuation and refilling of the inner accretion disk (e.g., Abramowicz et al. 1988; Belloni et al. 1997; Merloni & Nayakshin 2006; Pan et al. 2022). Currently, it has only been observed in two BHXRBs, GRS 1915 + 105 (hereafter, GRS 1915; Belloni et al. 1997; Neilsen et al. 2011) and IGR J17091–3624 (hereafter, IGR J17091; Altamirano et al. 2011; Court et al. 2017). Other types of accreting systems have also been observed to exhibit similar quasiperiodic flares, which are related to disk behaviors, such as the ultraluminous X-ray source, NGC 3621 (Motta et al. 2020), and one neutron-star X-ray binary, Swift J1858.6–0814 (Vincentelli et al. 2023).

IGR J17091 is a galactic low-mass BHXRB discovered with INTEGRAL/IBIS in 2003 April (Kuulkers et al. 2003). Later on, IGR J17091 had experienced another four typical outbursts in 2007, 2011, 2016, and 2022 (Capitanio et al. 2009; Krimm et al. 2011; Miller et al. 2016, 2022). As a comparison to GRS 1915, IGR J17091 was assumed to emit close to the Eddington luminosity, which implied either the BH has mass $<3\,M_\odot$ or the system could be farther away than 20 kpc (Altamirano et al. 2011). In previous studies, ten classes of variability have been identified by Court et al. (2017) and Wang et al. (2024). Among them, two classes of the variability had been detected in the most recent outburst in 2022 (Wang et al. 2024). Moreover, this outburst has been detected in multiwavelength from radio to X-ray with the telescopes including ATCA, NEOWISE, Swift, Fermi, NICER, and NuSTAR. Hence, the multiwavelength data set of IGR J17091 makes it an ideal candidate for investigating the origin of the nonthermal emission in BHXRBs.

In this study, we present an analysis of the 2022 outburst of IGR J17091 using the telescopes outlined above. Our specific objectives include studying the properties of the heartbeat-like variability and constraining the origin of the nonthermal

emission during the heartbeat state. Specifically, we describe the observation and data reduction procedures in Section 2, present the results of X-ray timing and spectral analysis along with a multiwavelength SED analysis in Section 3, discuss the implications of our results in Section 4, and finally summarize in Section 5.

2. Observations and Data Reduction

2.1. NuSTAR

During 2022, eight NuSTAR observations of IGR J17091 had been conducted (PI: J. Wang and J. Garcia), with a summary provided in Table 1. We conducted data processing using the NuSTAR Data Analysis Software (NUSTARDAS) version 1.9.7 with the Calibration Database version v20230420. We used the command *nupipeline* to calibrate the data with the arguments *saamode=strict*, *tentacle=yes*, and *statusexpr=(STATUS==b0000xxx00xxxx000)&& (SHIELD==0)*. We generated the source spectra and lightcurves for FPMA and FPMB in the energy range 3–50 keV, respectively, along with their corresponding response and ancillary response files, using the *nuproducts* task. The extraction of the source region is circled with a radius of $100''$, where the center is set at the emission peak by the *centroid* task. The background is chosen by placing a circular region at the farthest corner of the image from the source center, with the same radius as the source region. For observation 80801324004, a portion of the region in the FPMA image is contaminated, though the contamination does not affect the source region. This contamination, however, could lead to an overestimation of the background. Since this issue did not appear in FPMB, we chose to use the background file from FPMB as the background for FPMA for spectral fitting.

2.2. NICER

We obtained a data set comprising 175 observations from the NICER telescope, spanning from 2022 March 14 to October 12. Standard calibration procedures and screening using the *nicerl2* task were applied to each observation. Subsequently, the lightcurves and spectra were generated with *nicerl3-lc*, and *nicerl3-spect* in which the background was estimated by the 3C50 tool (Remillard et al. 2022). The processing pipeline used the NICER CALDB Version xti20221001.

2.3. Swift

The Swift/Burst Alert Telescope (BAT) daily lightcurves were directly downloaded from the Swift/BAT Hard X-ray Transient Monitor[12] (Krimm et al. 2013). The Swift/X-ray Telescope (XRT) lightcurves were generated by the online tools at UK Swift Science Data Centre[13] (Evans et al. 2007, 2009).

Regarding the Swift-UVOT observations, we combined their sky images and exposure maps using the *uvotimsum* task for each filter, and generated the count rates using the *uvotsource* task with the UVOT calibration 20220705. The source region was placed at the center of the X-ray emission region with a radius of $5''$. We carefully avoided any nearby sources and selected three background regions, each with a radius of $10''$. However, no significant source was detected, and we therefore

---

[12] https://swift.gsfc.nasa.gov/results/transients/
[13] https://www.swift.ac.uk/user_objects/

set a 3σ photometry upper limit at the source region of IGR J17091.

2.4. Fermi

Following the official users's guide,[14] we performed a binned analysis using FERMITOOLS 2.2.0 and the Pass 8 data covering MJD 59731–59832. We used the gtlike tool to conduct the spectral analysis, during which we fixed parameters to the 4FGL-DR4 catalog values, except for the normalization of sources within $3°$ of our target. In addition, since IGR J17091 is not in the 4FGL-DR4 catalog, we included it manually assuming a power-law spectrum with a photon index of two. This resulted in a low TS value for IGR J17091, suggesting that it was not detected significantly. Then we estimated its 0.1–10 GeV flux upper limit $F_{0.1-10\,\mathrm{GeV}} = 3.3 \times 10^{-11}\,\mathrm{erg\,cm^{-2}\,s^{-1}}$ using the UpperLimits[15] tool assuming a 3σ confidence level.

2.5. NEOWISE

We searched for the NEOWISE archive data from 2022 for the infrared detection in the location of IRG J17091. The W1 and W2 images were downloaded from the NASA/IPAC Infrared Science Archive[16] (NEOWISE-R Team 2020). Unfortunately, our target was not significantly detected by NEOWISE in single visits. Hence, we stacked the images from 2022 August as the source and the images from 2019 to 2021, when the target was in quiescent state, as the background. Both of the images were selected within a circular region with a radius of $10''$. Eventually, we derived the absorbed fluxes $F_{\mathrm{w1}} = 1.41 \pm 0.54$ mJy and $F_{\mathrm{w2}} = 0.68 \pm 0.59$ mJy.

Each X-ray spectral data were grouped using the *grppha* task from FTOOLS package (Blackburn 1995) to achieve a minimum of 30 counts per bin, as the requirements for χ^2 statistics. In our SED analysis, we apply the Fitzpatrick (1999) dust extinction model with $E(B - V) = 3.48$ (Planck Collaboration et al. 2016) from the infrared to UV band. We adopt the tbabs component to account for the interstellar absorption, using the *abund wilm* command to set the abundance table (Wilms et al. 2000) and *xsect vern* command to set the photoelectric cross sections (Verner et al. 1996). We fix the equivalent hydrogen column density at $N_{\mathrm{H}} = 1.537 \times 10^{22}\,\mathrm{cm}^{-2}$, as measured by the NICER observations in 2022 (Wang et al. 2024). Unless explicitly mentioned, the uncertainties for each fitting parameter in this work were calculated at 1σ confidence level.

3. Result

3.1. Timing Analysis

3.1.1. Lightcurves

Figure 1 shows the lightcurves of IGR J17091 in the studied period, as observed with NICER, NuSTAR, and Swift-XRT/BAT. We calculated the fractional rms (Vaughan et al. 2003) for the NICER's daily lightcurve with a time bin of 1 s to provide a general evolution of the variability amplitude, which indicates an intermittent occurrence of variability. Additionally, we observed quasiperiodic variability from the lightcurve in

NuSTAR observations ObsIDs 80702315004 (hereafter NV-1), 80702315006 (hereafter NV-2), and 80802321003 (hereafter NV-3), while during the two-day observation, ObsID. 80801324004 (hereafter NV-4), the variability was intermittent. Therefore, we only studied the observation segments of NV-4 where the variability persists for longer than 2000 s. In this work, we refer to the variability with a period of tens of seconds and a time lag of seconds as "heartbeat-like" variability (see Section 3.1.2 for more details).

3.1.2. Power Spectrum and Cross Spectrum

In our timing analysis, we used the *AveragedPowerspectrum* and *AveragedCrossspectrum* packages in *Stingray* (Huppenkothen et al. 2019a, 2019b) to generate the average power/cross spectra (PS/CS) from the lightcurves. We used the real part of the CS as the cospectrum (Bachetti et al. 2015). We applied logarithmic rebin with a factor of 0.01 and adopted the normalization with the fractional rms method (Belloni & Hasinger 1990). For the NuSTAR data, the cospectrum was generated over an energy range of 3–50 keV between FPMA and FPMB, with a time step of $\delta t = 0.1$ s and a segment length of $T = 500$ s. We further averaged the cospectrum from each segment when there was no obvious shift in the frequencies of the main features of the cospectrum. The shift confined within the full width at half-maximum (FWHM), denoted as $\Delta\nu$, is considered acceptable. To describe the cospectrum, we used the *ftflx2xsp*[17] task in the FTOOLS package (Blackburn 1995) to convert each cospectrum data point into spectra and response formats for fitting in XSPEC (Arnaud 1996). We fitted the cospectrum by iteratively adding Lorentzian components until no prominent features remained in the residuals and the χ^2 value was not significantly further improved. However, we found that NV-4 exhibits a significant shift in ν_c from 16 to 27 mHz during the observation. Therefore, we included only the data for which the cospectrum met the above criteria with no obvious shift in ν_c, for the subsequent timing analysis. The Lorentzian component with the strongest power at ν_c was identified as the fundamental component of heartbeat-like variability. The fractional rms of the Lorentzian component was calculated by taking the square root of the Lorentz normalization factor, and a correction was applied to obtain the intrinsic rms using Equation (5) from Bachetti et al. (2015). The middle panels in Figure 2 display the Lorentz fitting results of the cospectrum in the 3–50 keV. The properties of the fundamental Lorentzian component are shown in Table 2. We also generated the PS from the NICER observations, where we noted that the heartbeat-like variability appears when the fractional rms is large, as shown in Figure 1.

According to the definition of the variability classes in GRS 1915 and IGR J17091 by Belloni et al. (2000), Altamirano et al. (2011), and Court et al. (2017), the heartbeat-like variability present in NV-2 and NV-4 corresponds to Class V and IV (or Class ρ), respectively. In addition, NV-3 is categorized as a new type of heartbeat-like variability, i.e., class X (Wang et al. 2024). The amplitude of the variability in NV-1 is too weak to be further identified.

To obtain the rms spectra for each observation, we generated lightcurves in smaller energy bands from the NuSTAR event file and constructed their cospectrum between FPMA and
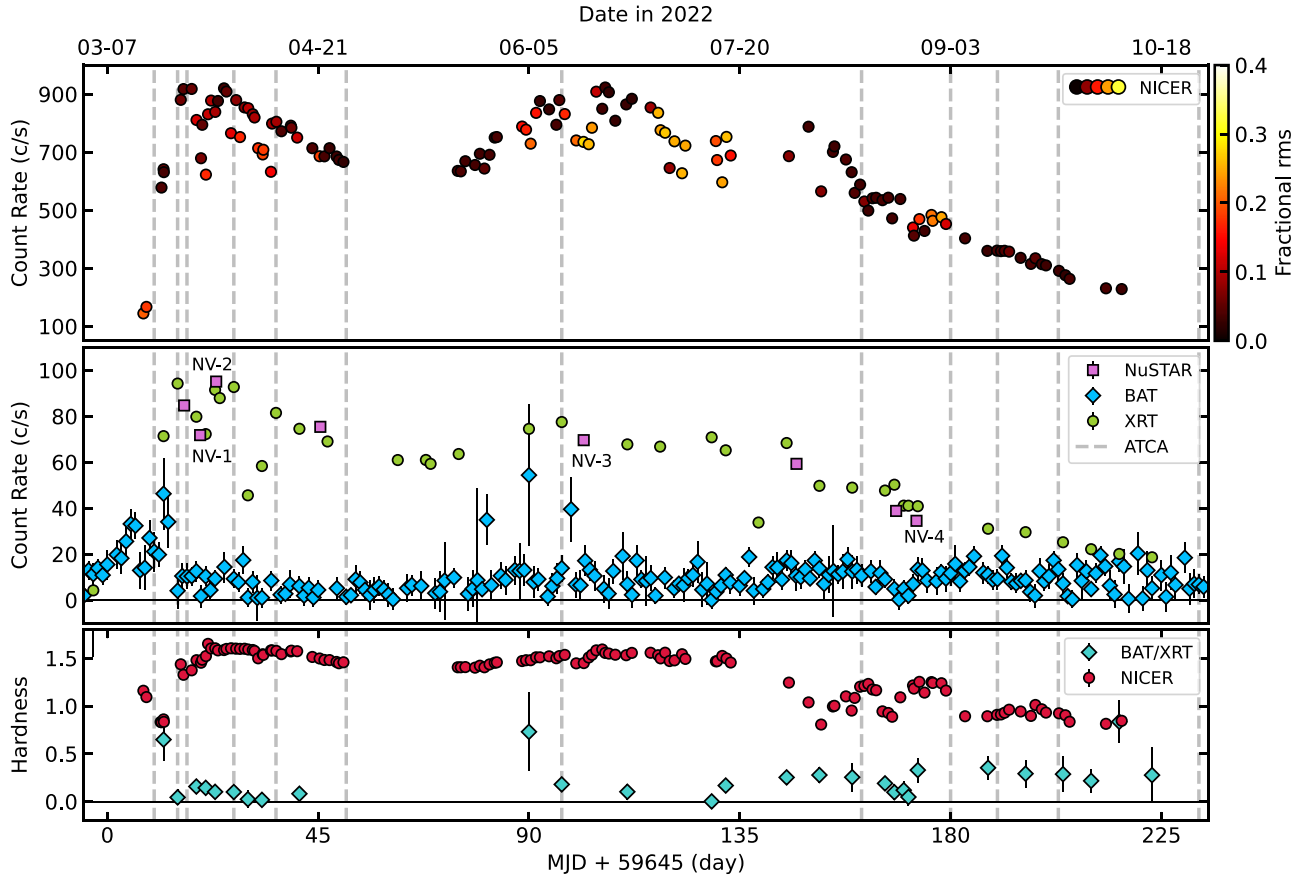

Figure 1. Top panel: the lightcurve of NICER during the 2022 outburst. The color bar represents the fractional rms (Vaughan et al. 2003) in the 1–10 keV band. Middle panel: the lightcurves of NuSTAR (magenta), Swift/XRT (green), and Swift/BAT (blue). The dashed vertical lines denote the observation times with ATCA. Bottom panel: the red circles and the cyan diamond represent the hardness ratio of NICER count rates in the 2–10 keV and the 1–2 keV energy ranges, and with Swift in the BAT (15–50 keV) and XRT (0.3–10 keV), respectively.

Table 1
Summary of the NuSTAR Observations of IGR J17091

ObsID	Date	Start Time (MJD)	Exp. A (ks)	Exp. B (ks)	Count Rate A (ct s^{-1})	Count Rate B (ct s^{-1})
80702315002	2022-03-23	59661.1693	14.8	15.0	84.7	77.7
80702315004 (NV-1)	2022-03-26	59664.5889	16.5	16.8	71.8	66.2
80702315006 (NV-2)	2022-03-29	59668.0149	11.9	11.3	95.1	87.8
80802321002	2022-04-21	59690.2104	17.6	17.8	75.4	69.3
80802321003 (NV-3)	2022-06-16	59746.4750	16.1	16.8	69.6	63.8
80802321005	2022-07-31	59791.8694	15.9	16.1	59.3	54.0
80801324002	2022-08-22	59813.0544	27.6	27.8	38.8	35.9
80801324004 (NV-4)	2022-08-25	59816.6805	75.8	78.6	34.5	31.9

FPMB. We linked ν_c and $\Delta\nu$ of each Lorentzian component to the values derived in the full band cospectrum, but left their Lorentzian normalization free to vary. At the energy band where the Lorentzian component was not significantly required, we provided a 3σ upper limit for its fractional rms. Regarding the lag spectra, we generated the CS/PS in the selected energy bands, where the Lorentzian component was significantly required, and used the 3–4 keV band as the reference band. We applied the constant time-lag model adopted from Méndez et al. (2024) to jointly fit the PS, and the real and imaginary parts of the CS to determine the time lags.

We show the evolution of rms and time lag with energy in Figure 3. The rms of NV-2, NV-3, and NV-4 share a similar trend: the rms increases with energy and then decreases after reaching an inflection energy, although the inflection energy differs among them. For NV-1, the rms spectrum remains nearly constant within the 3–10 keV band. The lag spectra in all observations show a positive (hard) lag of several seconds below 15 keV, while for NV-3 and NV-4, they change sign from positive to negative above 15 keV. Additionally, we detected a hump at ~28 mHz in the lag spectrum of NV-3, which could be explained by a Lorentzian component at $\nu_c = 28$ mHz in the cospectrum of NV-3. To distinguish it from
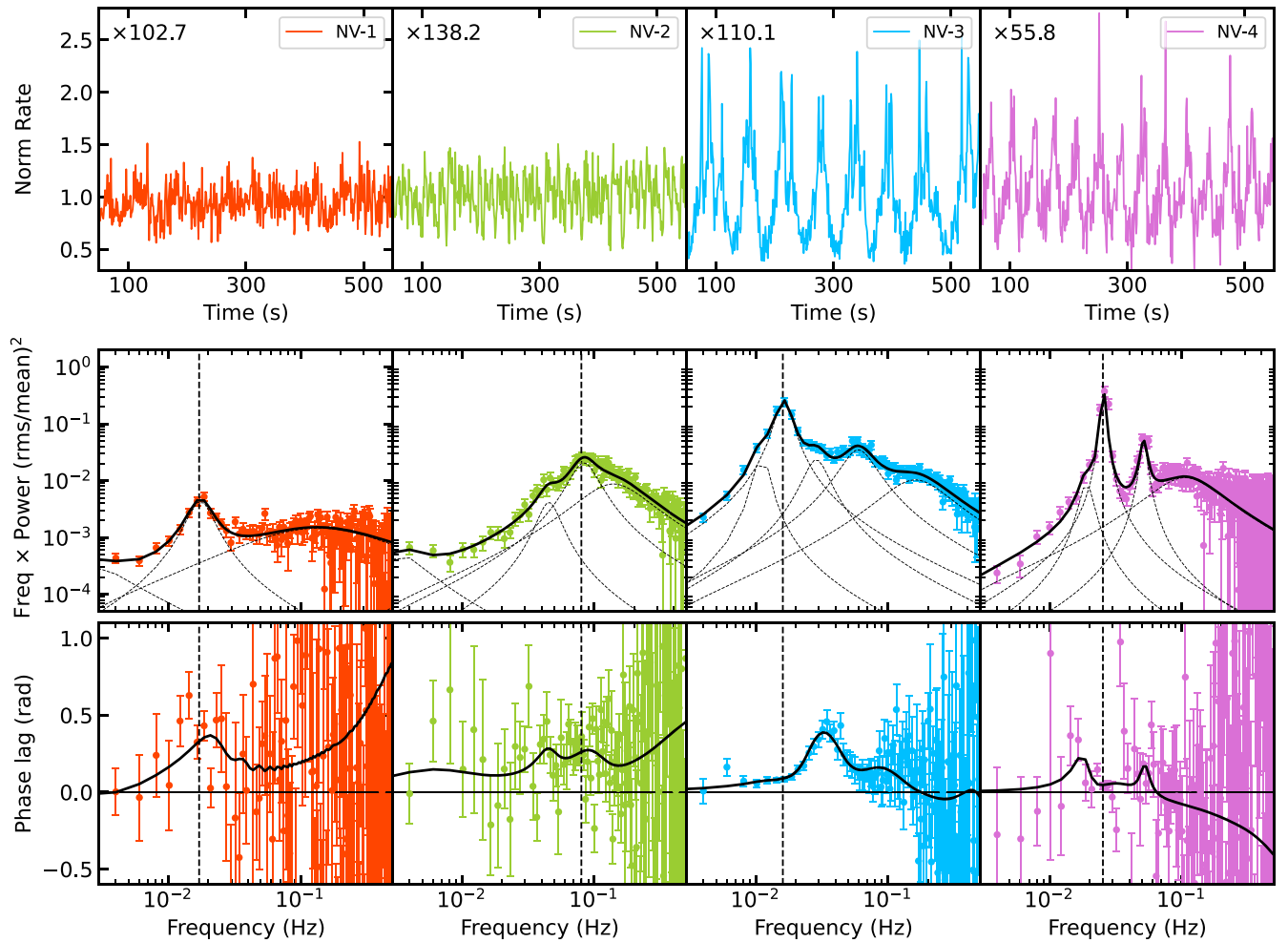
Figure 2. Top panel: normalized lightcurves of the four NuSTAR observations in FPMA (NV-1 in red, NV-2 in green, NV-3 in blue, and NV-4 in magenta). The normalization factor of the count rate is shown in the top-left corner. Middle panel: the cospectrum between FPMA and FPMB in the energy band 3–50 keV. The black solid curve denotes the overall best-fitting model, and each dashed curve corresponds to an individual Lorentz component. The vertical dashed line marks the centroid frequency ν_c of the heartbeat-like variability. Bottom panel: the phase lag spectrum between 3–4 keV (reference band) and 7–10 keV. The black solid curve indicates the best-fitting result of the constant time-lag model (Méndez et al. 2024).

Table 2
Properties of the Heartbeat-like Variability Derived from the Cross Spectrum

ObsID	Class	ν_c (mHz)	$\Delta\nu$ (mHz)	rms (%)	Time Lag[a] (s)
80702315004 (NV-1)	⋯	17.1 ± 0.3	7.1 ± 1.1	6.6 ± 0.3	3.7 ± 0.6
80702315006 (NV-2)	V	79.8 ± 2.0	37.0 ± 7.9	15.7 ± 1.8	0.6 ± 0.1
80802321003 (NV-3)	X	16.0 ± 0.2	4.1 ± 0.4	42.2 ± 1.7	0.9 ± 0.1
80801324004 (NV-4)	IV	25.3 ± 0.2	1.1 ± 0.2	25.9 ± 1.7	0.3 ± 0.1
80802321003 (NV-3B)	⋯	28.0 ± 0.5	11.8 ± 1.3	15.3 ± 1.3	2.9 ± 0.3

Note.
[a] The time lag is calculated between 3–4 keV and 7–10 keV. A positive value means that high-energy photons arrive after low-energy ones.

the fundamental heartbeat-like component, we define this component as NV-3B. This component exhibits different evolutionary patterns in both rms and lag spectra from NV-3, but it shares similarities with the variability in NV-1.

Overall, the heartbeat-like variability in the hard energy band (above 20 keV) has been observed to be either nonexistent (for NV-1 to NV-3) or very weakly detected (for NV-4) compared to the soft energy band (below 20 keV). This possibly suggests an inefficient propagation between soft and hard photons.

3.2. Spectral Analysis

In the following, we conduct an analysis using average and phase-resolved spectra to further investigate the origin of the nonthermal X-ray emission.

3.2.1. Average spectra

The spectra were analyzed using XSPEC version 12.12.1 (Arnaud 1996). We conducted spectral fitting for IGR J17091
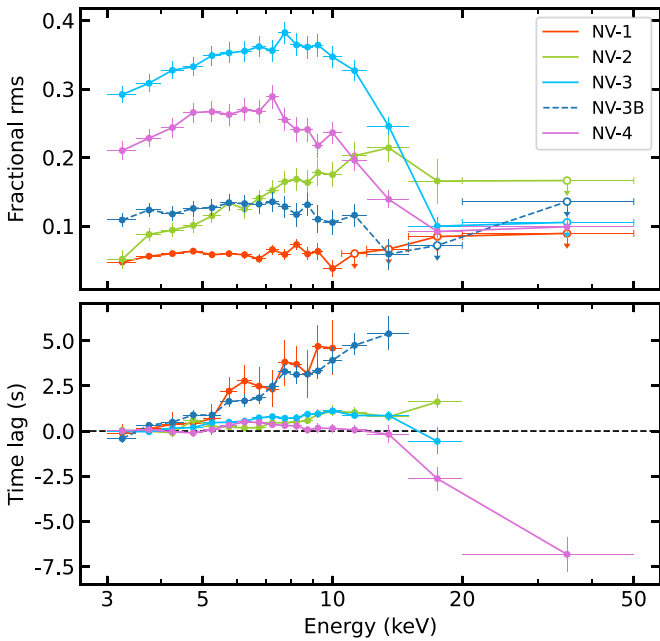
Figure 3. Upper panel: the rms spectra of NuSTAR data. The solid curve is the fundamental Lorentzian component, while the dashed, dark-blue curve is the NV-3B. The open circles mark the 3σ upper limit, where the Lorentz component is not significantly required. Lower panel: the lag spectra of NuSTAR data. The inset plot in the lower-left corner provides a closer view along both the x- and y-axes.

using NuSTAR data in the energy range of 3–50 keV. We used an absorbed multicolor blackbody component `diskbb` (Mitsuda et al. 1984) convolved by a `thcomp` model (Zdziarski et al. 2020) to describe the disk emission and the inverse Compton scattering of the disk photons. We extended the energy range using the command *energies 0.01 1000.0 1000 log*. A multiplicative `constant` parameter was used to account for crossnormalization of the FPMA and FPMB instruments, where we fixed this to 1 for the FPMA and left it free for FPMB. The model is `constant×tbabs×(th-comp×diskbb)`. However, despite the reduced χ^2 values ranging from 1.04 to 1.28, which appear marginally acceptable, there are still noticeable residuals in either the soft or the hard bands, as illustrated in the upper panels of Figure 4. To improve the fit, we incorporated a `powerlaw` component, which reduced the χ^2 values to a range of 1.00–1.04 (see the lower panel of Figure 4). We further ran F-test to examine the significance of this `powerlaw` component, and obtained a p-value less than 10^{-5}. This confirms that the inclusion of the additional `powerlaw` component is indeed necessary. The overall model is `tbabs×(thcomp×diskbb + powerlaw)`, as showed in Figure 5.

As the `thcomp` component is convolved with the `diskbb` component, it represents an inverse Comptonization process occurring in the corona. To investigate whether the `powerlaw` component is associated with the variability, we conducted phase-resolved spectroscopy.

3.2.2. Phase-resolved Spectra

Due to the low rms amplitude and the high $\Delta\nu$ (see Table 2) of the variability in NV-1 and NV-2, it is difficult to accurately determine the variability profile from their lightcurves and

hence the phase. Thus, we only did phase-resolved spectroscopy for NV-3 and NV-4. To eliminate the noise contribution to the heartbeat-like variability, we applied an optimal filtering algorithm to the fundamental Lorentz component of NV-3 and NV-4 (see Table 2) in the 3–50 keV lightcurve, as described by van den Eijnden et al. (2016). We then used the *find_peaks* package from the *scipy* (Virtanen et al. 2020) library to identify dips within each sine-like pattern present in the filtered lightcurve. The nearest two dips were designated as phases $\phi = 0$ and $\phi = 2\pi$. We finally folded the original lightcurve and assigned five phases accordingly.

We fitted the phase-resolved spectra with the same model as used for fitting the average spectra, i.e., `constant×t-babs×(thcomp×diskbb + powerlaw)`. Due to the limitation of the statistics, we jointly fitted the average and the phase-resolved spectra for NV-3 and NV-4 to improve the constraints on the parameters. To examine the variation of each parameter across different phases, we linked each parameter and quantitatively assessed their respective changes by χ^2 values. We find that linking the `powerlaw` component and the electron temperature (kT_e) in `thcomp` across different phases does not significantly affect the χ^2 values. Hence, we linked the `powerlaw` component and kT_e among each phase. This approach resulted in a slight increase in the χ^2, i.e., $\Delta\chi^2 = 25.0$ for 15 additional degrees of freedom (dof) in NV-3 and $\Delta\chi^2 = 31.5$ for 15 additional dof in NV-4. Thus, these results indicate that the `powerlaw` component and kT_e in `thcomp` do not exhibit significant variations across different phases. We also calculated the flux for each component from the fits to both the average and the phase-resolved spectra with the command *cflux*.

The best-fitting parameters of the average spectrum for each observation are presented in Table 3, and the corresponding spectra, as well as the residuals, are shown in Figure 5. We observe a high disk temperature ($T_{in} > 1.3$ keV) and a low electron temperature of the corona ($kT_e < 10$ keV) during the heartbeat-like variability. We show the best-fitting parameters derived from the phase-resolved spectroscopy as a function of phase in Figures 6. The folded lightcurve of NV-3 presents a profile characterized by a rapid rise and slow decay, whereas NV-4 displays a slow rise and a rapid decay. In both NV-3 and NV-4, the evolution of the disk temperature aligns with the lightcurve profile. In addition, the flux difference between the peak and dip phases in `diskbb` is about five times greater than in `thcomp`, implying that the heartbeat-like variability is dominated by the accretion disk.

3.2.3. Multiwavelength SED

The results above suggest that at least part of the nonthermal emission, i.e., the `powerlaw` component, may not be associated with the thermally originated heartbeat-like variability, and hence not be attributed to the inverse Comptonization of the disk photons. To investigate whether this component could originate from jets, we conducted a broadband SED fitting spanning from radio to X-rays.

ATCA observed IGR J17091 several times in 2022 with the dates marked by the vertical dashed lines in Figure 1. Only two of them, 2022 June 12 (Projects: C3456) and 2022 September 3 (Projects: CX501), were quasisimultaneous with our well-defined heartbeat-like variability in NV-3 and NV-4. According to the flux density measured by T. D. Russell et al. (2024, in preparation), IGR J17091 was not detected on June 12, with 3σ upper limits of 126 μJy at 5.5 GHz and 106 μJy at 9 GHz. On
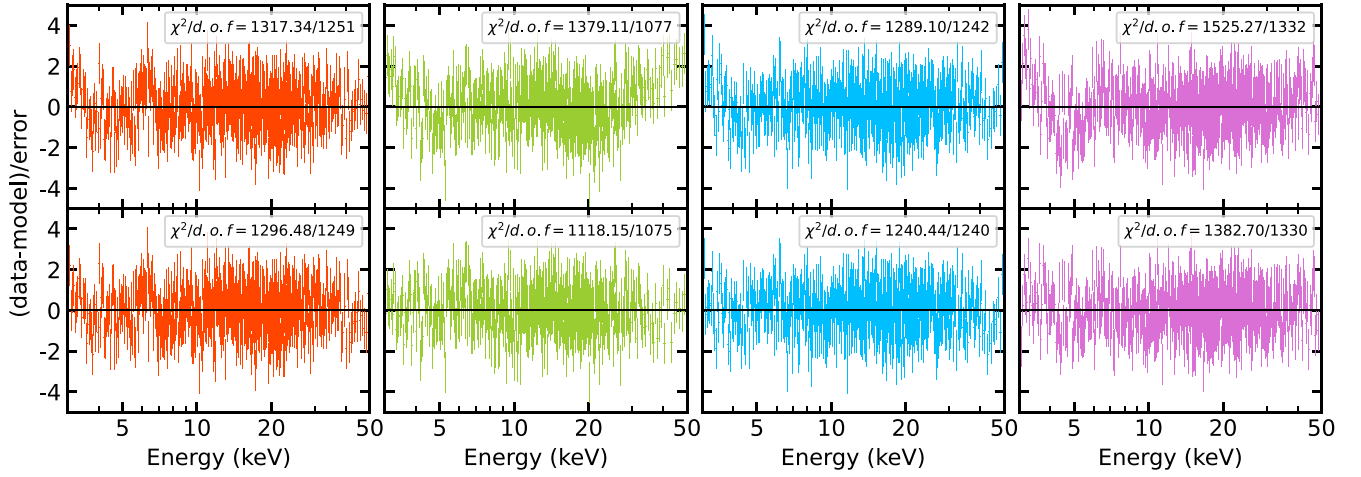
Figure 4. Top panel: residuals in FPMA from NuSTAR spectral fitting using the model `constant×tbabs×(thcomp×diskbb)`. The panels from left to right represent NV-1, NV-2, NV-3, and NV-4. The top-right value in each panel denotes the reduced χ^2 for each fit. Bottom panel: residuals in FPMA from NuSTAR spectral fitting using the model `constant×tbabs×(thcomp×diskbb + powerlaw)`.
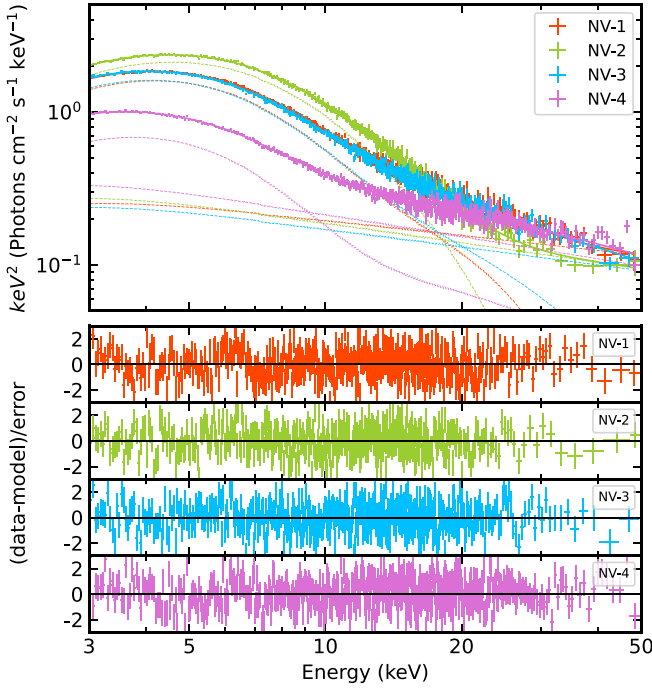
Figure 5. The unfolded NuSTAR spectra for FPMA and the corresponding residuals. The colors are defined the same as in Figure 2. The spectra of NV-1 and NV-3 overlap on the plot.

the other hand, IGR J17091 was detected on September 3, with a flux density of $170 \pm 35\ \mu$Jy at 5.5 GHz and $151 \pm 38\ \mu$Jy at 9 GHz, respectively. The ATCA detection on September 3 was used in our SED fitting.

To extract the `powerlaw` component from the X-ray spectrum, we subtracted the contribution from the `thcomp×diskbb` component from the NuSTAR data and divided it with `tbabs`, using the best-fitting parameters from Table 3. Since we only fitted the continuous broadband spectrum, the NuSTAR data were further rebinned by a factor of 0.1 in logarithmic space. Moreover, due to the uncertainties in dust extinction and potential measurement bias in the infrared photometry, we excluded it from the SED analysis below. However, we used it together with the upper limits of the Swift-UVOT and Fermi data to evaluate the overall fit. We

considered a leptonic jet model to fit and interpret the radio and X-ray data. For this, we used the open-source *JetSeT*[18] framework (Tramacere et al. 2009, 2011; Tramacere 2020), which includes the synchrotron and SSC processes.

In the adopted jet model, we considered a basic assumption of power-law energy distribution of relativistic electrons. This leads to eight parameters in the model: the minimum Lorentz factor, $\gamma_{\min}$, the minimum Lorentz factor, $\gamma_{\max}$, the spectral index of relativistic electrons distribution, p, the Doppler beaming factor, δ_D, the magnetic field intensity B, the radius of the emitting blob, R, the total electron number density in the blob, N_e, and the luminosity distance, D.[19]

The further setup for the model is as follows. Considering the previous measurements of the viewing angle, $\theta = 45°.3 \pm 0°.7$ (Wang et al. 2018) and $\theta = 24° \pm 4°$ (Wang et al. 2024), which suggests a Doppler beaming factor $\delta_D < 2.5$, we initially adopted the Doppler factor of $\delta_D = 1$. According to particle acceleration simulations (e.g., Sironi & Spitkovsky 2011, 2014), we chose $\gamma_{\min} \leqslant 100$. Regarding $\gamma_{\max}$, previous studies suggest that jets can be efficient at accelerating particles to energies above 10 GeV in microquasars (e.g., Bosch-Ramon & Khangulyan 2009; Molina et al. 2019; Harvey et al. 2022), and hence $\gamma_{\max} = 10^5$ is adopted. This enables the SED to extend up to energies of ≈ 50 GeV, within the Fermi range. The luminosity distance of IGR J17091 is still uncertain. Here, we adopted a luminosity distance of 13.7 kpc, estimated from the radio–X-ray relationship (see Section 4.3 for details). Ultimately, we are left with five free parameters for the fitting process: $\gamma_{\min}$, p, B, R, and N_e.

Moreover, we used the *Minuit ModelMinimizer* (James & Roos 1975) option in *JetSeT* to provide initial values for the model parameters, and used the Monte Carlo Markov Chain (MCMC) ensemble sampler (Foreman-Mackey et al. 2013) to achieve a robust fit. This involves initializing 50 walkers to solve the maximum likelihood solution and exploring the parameter space with 10^4 steps each. The parameter B, R, and N_e were set in log-scale during the fitting.

Upon the fit, we obtain $p = 3.88 \pm 0.09$, consistent with the result shown in Table 3, where $\Gamma_{\text{po}} = (p+1)/2$. If further assuming that both radio and X-ray emissions originate from

---

[18] https://jetset.readthedocs.io/en/latest/
[19] The original parameter required by the *JetSeT* model is the cosmological redshift. We converted it to the luminosity distance here.

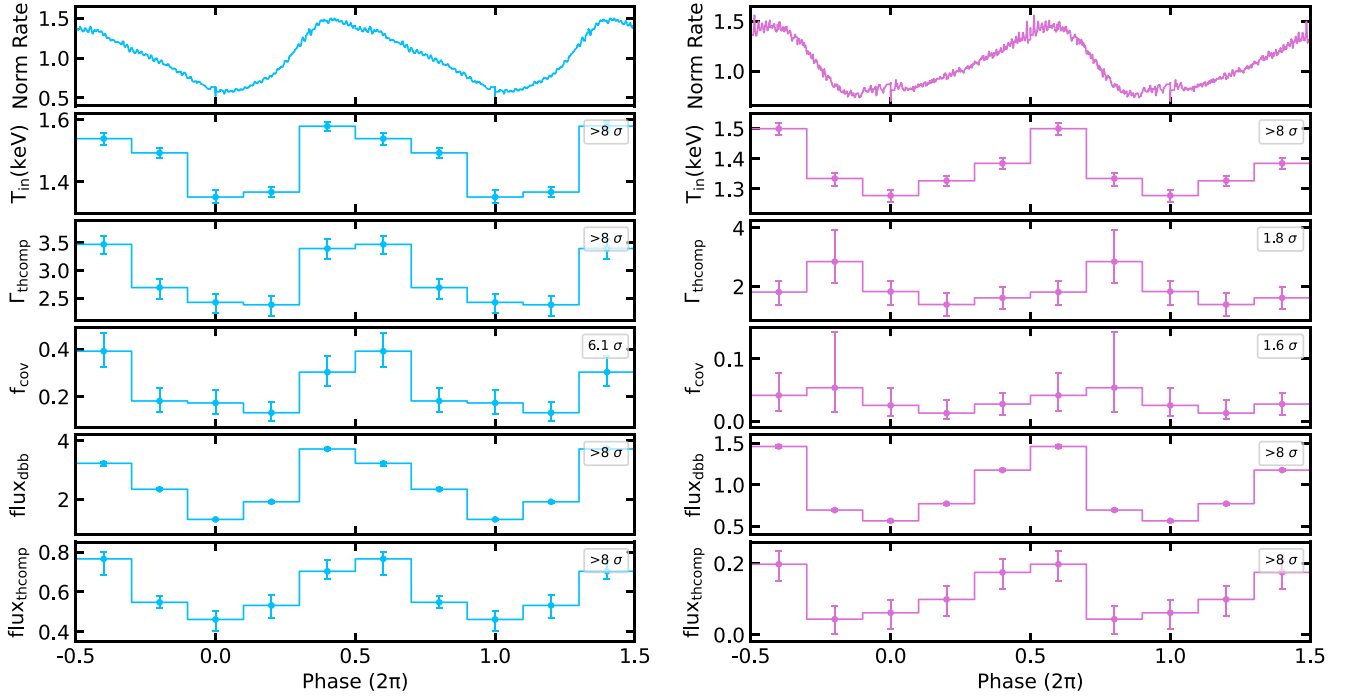**Figure 6.** Best-fitting parameters from phase-resolved spectra of NV-3 and NV-4 using the model `constant×tbabs×(thcomp×diskbb + powerlaw)`. The panels from top to bottom show the normalized count rate, the disk temperature, the photon index of `thcomp`, the covering fraction, the unabsorbed flux of `diskbb`, and the unabsorbed flux of `thcomp`. The legend in the top-right corner shows the significance of parameter variations, assessed by allowing the parameters to vary freely and linking them across all phases using the F-test.

Table 3
Best-fitting Parameters of the NuSTAR Spectra of IGR J17091

Parameters	NuSTAR ObsID			
	80702315004 NV-1	80702315006 NV-2	80802321003 NV-3[a]	80801324004 NV-4[a]
C_{FPMB} [b]	0.992 ± 0.001	0.988 ± 0.001	0.981 ± 0.001	0.987 ± 0.001
N_{H} (cm^{-2})[c]		1.537×10^{22}		
T_{in} (keV)	$1.57^{+0.04}_{-0.03}$	$1.70^{+0.03}_{-0.04}$	1.47 ± 0.01	1.38 ± 0.02
N_{dbb}	$41.2^{+3.8}_{-4.1}$	$37.8^{+3.1}_{-2.3}$	$52.6^{+2.4}_{-2.4}$	$28.5^{+2.0}_{-1.7}$
Γ_{thcomp}	$1.7^{+0.5}_{-0.7}$[d]	$1.3^{+0.8}_{-0.3}$[d]	$2.9^{+0.1}_{-0.2}$	$1.7^{+0.3}_{-0.4}$
kT_{e} (keV)	$3.8^{+0.9}_{-0.6}$	$2.5^{+0.3}_{-0.1}$	$9.4^{+6.0}_{-2.6}$	$4.5^{+1.2}_{-0.6}$
f_{cov}	$0.05^{+0.06}_{-0.04}$	$0.03^{+0.14}_{-0.02}$	0.3 ± 0.1	0.03 ± 0.02
Γ_{pl}	2.3 ± 0.1	2.4 ± 0.1	2.4 ± 0.1	2.46 ± 0.01
N_{pl}	0.4 ± 0.1	0.5 ± 0.1	0.4 ± 0.1	$0.73^{+0.04}_{-0.05}$
F_{dbb} [e]	$2.55^{+0.06}_{-0.03}$	3.5 ± 0.1	$2.40^{+0.01}_{-0.03}$	0.91 ± 0.01
F_{thcomp} [e]	0.4 ± 0.1	0.6 ± 0.1	0.6 ± 0.1	$0.13^{+0.04}_{-0.03}$
F_{pl} [e]	0.86 ± 0.04	0.8 ± 0.1	$0.7^{+0.1}_{-0.2}$	1.11 ± 0.04
χ^2/dof	1296.5/1249 (1.04)	1118.2/1075 (1.04)	5126.6/5025 (1.02)	5948.6/5832 (1.02)

Notes.
[a] The results for NV-3 and NV-4 are obtained through the joint fitting of the average and phase-resolved spectra.
[b] The constant parameter for FPMA is fixed at 1.
[c] N_{H} is adopted from Wang et al. (2024).
[d] Γ_{th} pegs at its hard limit of 1.001.
[e] The unabsorbed flux is in units of 10^{-9} erg cm^{-2} s^{-1}.

the same synchrotron process (referred to as case (a) subsequently), we constrain $R > 10^{12}$ cm and $N_e < 5\,cm^{-3}$, though both parameters are correlated as $N_e R^3 \approx 1.2 \times 10^{36}$ (shown in the cornerplot in Figure A1). The values of γ_{min} and B are also related as $B \approx 4.5 \times 10^7 \left(\frac{10}{\gamma_{\mathrm{min}}}\right)^2$ G (also seen in Figure A1). As $1.1 < \gamma_{\mathrm{min}} < 100$, B would be in the range of

10^5–10^9 G. We show the best-fitting SED in Figure 7 and the parameter distributions in the left panel of Figure A1.

However, this assumption results in a very large magnetic energy, $E_B \sim B^2 R^3/6 > 3 \times 10^{46}$–$10^{54}$ erg, which seems to be impractical in a BHXRB. This also leads to an extremely large ratio between the magnetic and electron energy densities, $U_B/U_e > 10^{10}$. Overall, we exclude the possibility that both the
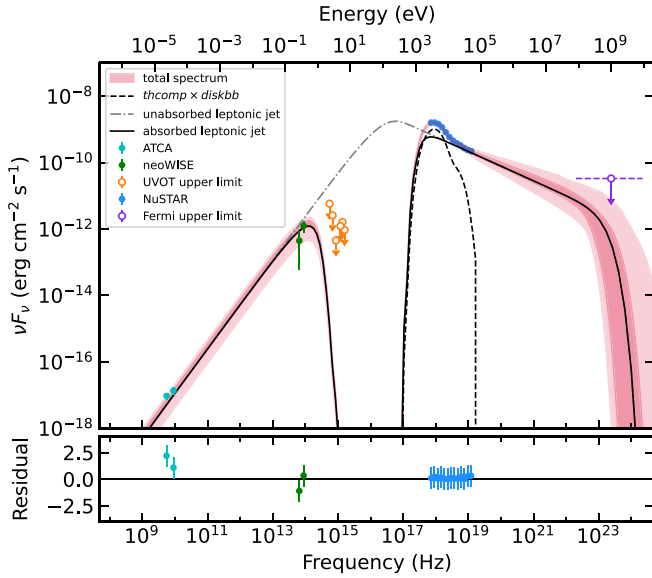
Figure 7. Top panel: absorbed SED fitted with a synchrotron model (case (a) in Section 3.2.3). The red region represents the total spectrum of the last 1000 steps of MCMC walkers within the 1σ and 3σ confidence intervals. The solid line shows the best-fitting absorbed leptonic jet model, while the dashed line corresponds to the thcomp×diskbb model. The data points are from ATCA (cyan), NEOWISE (green), UVOT (orange), NuSTAR (blue), and Fermi-LAT (purple). The horizontal purple dashed line on the Fermi-LAT data represents the instrument's energy range. The broad gap from 10^{15} to 10^{17} Hz is due to high extinction, and the unabsorbed leptonic jet model is plotted as the gray dashed–dotted line. Bottom panel: residuals of the best-fitting model.

radio and X-ray emissions observed in IGR J17091 originate from the same synchrotron process.

We then consider two other cases: (b) the X-ray emission is produced by synchrotron processes in a compact spherical blob, whereas the radio emission comes from a more expanding region, and (c) the same as above but the X-ray emission is from SSC. We note that these two possibilities would require a multizone jet model (e.g., Kaiser 2006; Kantzas et al. 2021; Lucchini et al. 2022; Tramacere et al. 2022), but for simplicity we neglect the fitting of the radio data which would constitute an upper limit to the compact blob emission, and focus only on the analysis of the high-energy emission within a one-zone approximation.

Here, we assume an energy equipartition condition, $U_B = U_e$. In this case, N_e is calculated as follows:

$$N_e = \frac{B^2}{8\pi m_e c^2} \times \frac{(\gamma_{\max}^{1-p} - \gamma_{\min}^{1-p})/(1-p)}{(\gamma_{\max}^{2-p} - \gamma_{\min}^{2-p})/(2-p)}. \tag{1}$$

The fitting allows for two sets of solutions, one with $\gamma_{\min} > 50$ that corresponds to case (b), and one with $\gamma_{\min} < 10$ that corresponds to case (c).

In case (b), the X-ray emission is dominated by synchrotron, while SSC dominates above 100 keV (see the upper panel of Figure 8). This fit then yields a gamma-ray flux of $F_{0.1-10\,\mathrm{GeV}} = 2.5^{+0.7}_{-0.8} \times 10^{-9}\,\mathrm{erg\,cm^{-2}\,s^{-1}}$, significantly exceeding the Fermi upper limit of $3.3 \times 10^{-11}\,\mathrm{erg\,cm^{-2}\,s^{-1}}$. Therefore, we disfavor this case.

In case (c), the X-ray emission should originate from SSC (see the lower panel of Figure 8). The obtained best-fitting parameters are $\gamma_{\min} < 6.4$, $p = 4.3 \pm 0.2$, $B = (0.3–3.5) \times 10^6\,\mathrm{G}$, and $R = (0.1–2.5) \times 10^8\,\mathrm{cm}$, where the parameters B

and R are actually correlated. Namely, the SSC flux is approximately $\propto BR^{-6/(p+5)}$ (Shidatsu et al. 2011), leading to $B \approx 9.3 \times 10^{10}\,R^{-0.65}\,\mathrm{G}$ (see the right panel of Figure A1). It is worth noting that variations in D (11–23 kpc) and δ_D (1–2.5) do not alter our conclusions.

Overall, our results favor case (c), where the X-ray emission in the jet originates from the SSC process within a compact blob with a strong magnetic field, while the radio emission arises from a more expanding region distinct from the X-ray-emitting region. A simple schematic of case (c) is provided in Figure 9.

4. Discussion

In this study, we undertake a comprehensive timing and spectral analysis of the heartbeat-like variability observed in IGR J17091 during the 2022 outburst. We employ this type of variability as an indirect method to differentiate the origins of nonthermal components emanating from the corona and jets. Our phase-resolved spectroscopy reveals the presence of a power-law component that remains uncorrelated with the heartbeat-like variability associated with the accretion disk. Here, we discuss the potential origins of this variability, the nature of the nonthermal components, and their broader implications.

4.1. The Origin of the Heartbeat-like Variability

As mentioned in Section 3.1, at least three classes of heartbeat-like variability were detected in the four studied NuSTAR observations. These variabilities exhibit a similar evolutionary pattern in the rms spectrum, where the rms initially increases with energy and then decreases at higher energies. Although the inflection energy varies among observations, this value appears to correlate with the disk behavior; specifically, a higher disk temperature and a larger disk flux ratio correspond to a higher inflection energy (see Figure 3 and Table 3). In the standard disk blackbody model, where the disk temperature (T_{in}) is proportional to the inner disk radius (R_{in}) raised to the power of $-3/4$ (e.g., Shakura & Sunyaev 1973; Makishima et al. 1986), fluctuations in R_{in} lead to changes in T_{in}. Consequently, this would result in a monotonic increase in the fractional rms with energy beyond T_{in}. The observed decrease in fractional rms at higher energy bands suggests the presence of an additional component, which is more prominent in flux and acts to dilute the variability originating from the disk.

Moreover, the detected time lag between 3–4 keV and energies above 5 keV is up to several seconds. Such a lag is at least 2 orders of magnitude larger than those observed for low-frequency QPOs (e.g., Zhang et al. 2017, 2020; Méndez et al. 2022; Nathan et al. 2022; Wang et al. 2022) and other types of variabilities at similar frequencies (e.g., Ma et al. 2021; Liu et al. 2022). Therefore, we can rule out the possibilities of geometry and intrinsic variability in the corona, light travel time between the disk and corona, and the inverse Compton scattering of disk photons in the corona (e.g., Zdziarski 1985; Miyamoto et al. 1988; Kara et al. 2019; Wang et al. 2022). However, the timescale of the lag is consistent with the order of the viscous timescale for matter transfer in the inner region of the disk (e.g., Mir et al. 2016). Combined with the correlation between the disk temperature and the count rate (Figure 6), all the evidence supports the
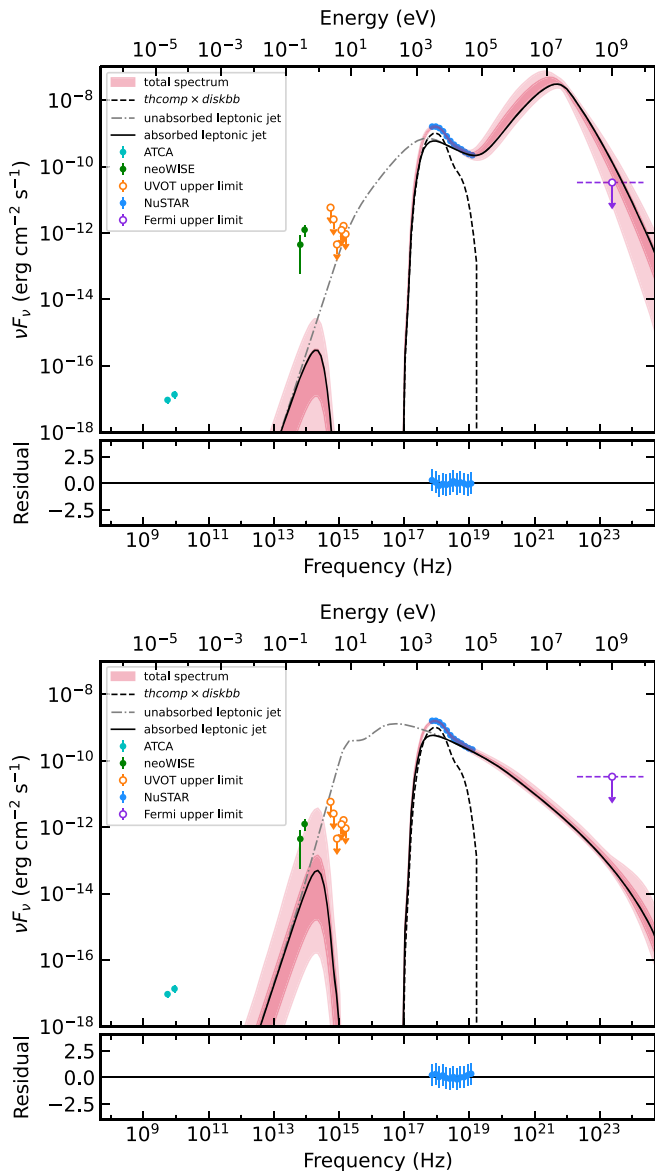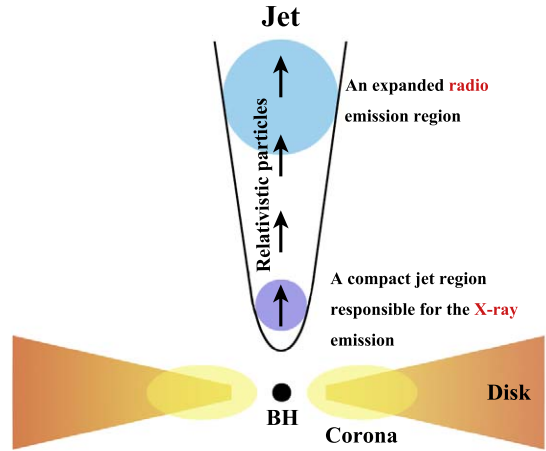
Figure 9. A schematic picture of the preferred case (c). The model consists of a multizone jet: around the base (the small purple region), the jet is optically thick at radio frequencies and the X-ray emission is produced via SSC; as the jet further expands, it becomes more transparent, eventually leading to the emergence of synchrotron radio emission (the large light-blue region).

4.2. The Origins of the Nonthermal Emission in XRBs

As discussed in Section 3.2.2, we observed a power-law component that is independent of the disk variability. Therefore, this component is unlikely to be driven by the inverse Compton scattering process between the disk photons and electrons in the corona. We therefore consider jets as the origin of the power-law component. In the jet, particles could move perpendicularly away from the accretion disk at relativistic speeds within a small solid angle (e.g., Pushkarev et al. 2009, 2017; Tetarenko et al. 2017; Miller-Jones et al. 2019; Zdziarski et al. 2022). This reduces the probability of particles in the jet scattering with disk photons, implying that photon propagation between the disk and jet is less efficient than between the disk and corona (e.g., Wilkins & Fabian 2012). This explains why the jet emission could vary independently from the disk emission in short timescales.

Furthermore, our multiwavelength SED fitting also favors the jet origin, where the X-ray emission is dominated by SSC radiation. This requires a compact blob with a radius of $R = (0.1–2.5) \times 10^8$ cm and a strong magnetic field of $B = (0.3–3.5) \times 10^6$ G. This magnetic field strength is larger than those typically measured in most BHXRBs, which are generally on the order of 10^4 G, as seen in systems like GX 339–4 (Shidatsu et al. 2011), XTE J1550–564 (Chaty et al. 2011), MAXI J1836–194 (Russell et al. 2014), Cygnus X–1 (Zdziarski et al. 2014), and MAXI J1535–571 (Russell et al. 2020). However, studies of MAXI J1820 + 070 (Rodi et al. 2021; Echiburú-Trujillo et al. 2024) and GRS 1915 + 105 (Punsly 2011) suggest that the launching region of the jet requires a magnetic field of $B \sim 10^5–10^7$ G, which is consistent with our results.

It is important to note that the decoupling between inverse Compton scattering from the corona and synchrotron+SSC radiation in the jet is model dependent. The alternative scenario, in which the nonthermal X-rays are dominated by inverse Compton scattering from the corona, cannot be ruled out. Related analyses supporting this perspective have been conducted by Draghis et al. (2024) and Wang et al. (2024).
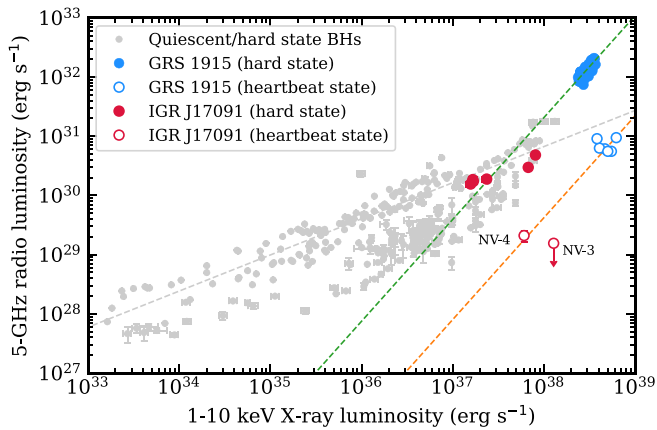
Figure 8. Absorbed SEDs and their residuals for cases (b) (top panel) and (c) (bottom panel) described in Section 3.2.3. The colors are the same as in Figure 7.

heartbeat-like variability originating from radiation pressure instabilities in the accretion disk (e.g., Janiuk et al. 2000; Nayakshin et al. 2000; Done et al. 2007).

Regarding the new type of variability, Class X, observed in NV-3, it actually exhibits a similar rms/lag evolution with that of Class IV in NV-4, but with higher rms below ~ 15 keV. Its folded lightcurve presents a profile characterized by a rapid rise and slow decay, opposite to NV-4. Interestingly, we observed a significant signal (NV-3B) in its lag spectrum, corresponding to a much weaker Lorentzian component at $\nu_c = 28 \pm 0.5$ mHz in the CS (see the light-blue data points in Figure 2). Furthermore, the lag/rms spectrum of NV-3B evolves differently from that of its fundamental component, i.e., NV-3 (Figure 3). All of these phenomena suggest that this additional variability may originate from a different emission region. However, further exploration is hindered by the nearby, dominant heartbeat-like variability in NV-3.

Figure 10. Radio–X-ray correlation for BHs. The gray points represent the data in quiescent/hard states. The gray dashed line has a slope of $\xi = 0.61$ while the green and orange dashed lines have a slope of $\xi = 1.72$. The distance of IGR J17091 is assumed to be 13.7 kpc.

4.3. Determining the Distance to IGR J17091

Due to the unusual types of variability shared by GRS 1915 and IGR J17091, it has been argued that the latter is a faint version of the former, either ascribed to a large distance or a smaller BH mass (e.g., Altamirano et al. 2011; Wang et al. 2018). However, owing to the high extinction in front of IGR J17091, its precise location and hence the central black hole mass are uncertain.

The logarithmic-linear relation between radio and X-ray emission has been verified in all types of accreting systems (e.g., Merloni et al. 2003; Corbel et al. 2013). GRS 1915 is situated in the top-right corner, beyond both the standard and hybrid radio–X-ray correlations for galactic BHs. Due to its extra-long outburst spanning over 26 yr (Neilsen et al. 2020), this deviation has been attributed to a high mass accretion rate in GRS 1915, while the similarities of GRS 1915 and IGR J17091 suggest that the two targets may share the same slope in the radio–X-ray fundamental plane.

We adopted the radio–X-ray fundamental plane for BHs from Bahramian & Rushton (2022) and plotted as gray dots in Figure 10. Additionally, we added both the radio and X-ray luminosities in the hard and heartbeat states of GRS 1915 as blue filled and open dots to the figure. The data in the hard state of GRS 1915 were adopted from Rushton et al. (2010), while the radio data in heartbeat states were adopted from Klein-Wolt et al. (2002). Regarding the X-ray data in the heartbeat state, we fitted each available RXTE spectrum with the model tbabs × (diskbb + powerlaw) to calculate the X-ray flux in the 1–10 keV band. For IGR J17091, we adopted the radio and X-ray data in the hard state from Rodriguez et al. (2011), Gatuzz et al. (2020), and Russell et al. (2022), while the data in the heartbeat state are from our study. To obtain the X-ray luminosities in the 1–10 keV band, we fitted the NICER spectra of IGR J17091 with the same model outlined above. The radio data are from the ATCA 5.5 GHz band.

As the data in the heartbeat state of GRS 1915 are rather scattered, we only measured the radio/X-ray slope, ξ, in the hard state and obtained $\xi = 1.72 \pm 0.13$, and assume that its heartbeat state shares the same slope as the hard state. The correlation track in the hard (green) and the heartbeat (orange) states of GRS 1915 is shown in Figure 10. We then applied these two correlation tracks to the data in the hard and the heartbeat states of IGR J17091, respectively, and used the least-

squares method to estimate its distance. We derived $D_{\mathrm{hard}} = 11.8^{+3.8}_{-2.9}$ kpc for the hard state and $D_{\mathrm{HB}} = 15.1 \pm 2.8$ kpc for the heartbeat state. By incorporating these into a joint probability distribution, we obtained the best-fitting distance to IGR J17091 to be $D = 13.7 \pm 2.3$ kpc. We adopt this distance to calculate the luminosity and plot the data of IGR J17091 as red dots in Figure 10. However, the new type of variability, class X, in NV-3 deviates from this relationship. This suggests that the emergence of this new type may require additional physical conditions to be met for activation.

5. Conclusions

In this work, we use archival data from NuSTAR, NICER, Swift, Fermi, NEOWISE, and ATCA to study the origin of the nonthermal X-ray emission in the heartbeat state during the 2022 outburst of IGR J17091. We find that the short-term variability arising from the accretion disk plays a crucial role in assessing and decoupling the contributions of the corona and the jet in the X-ray band.

Regarding the newly identified type of variability, Class X, although it presents a lightcurve profile opposite to that of Class IV, both can be driven by radiation pressure instability in the accretion disk. Moreover, we observed a significant component in the lag-frequency spectrum of Class X. This component exhibits different evolutions in both the rms and lag energy spectra compared to Class X, suggesting it may involve a separate emission region contributing to another form of quasiperiodic variability in X-rays.

Moreover, we suggest the distance to IGR J17091 of $D = 13.7 \pm 2.3$ kpc by assuming it shares the same radio–X-ray fundamental plane relationship as GRS 1915 during both the hard state and heartbeat states.

In X-ray timing and spectral analysis, we observe a power-law component that is independent of the heartbeat-like variability. Further quasisimultaneous broadband SED analysis suggests that this power-law component in the X-ray can be explained by SSC radiation within a compact blob, sized $R = (0.1–2.5) \times 10^8$ cm. This requires a strong magnetic field of $B = (0.3–3.5) \times 10^6$ G. In this case, our SED fitting suggests that the radio emission originates from a different region than the X-ray jet, consistent with the multizone jet model (e.g., Kaiser 2006; Kantzas et al. 2021; Lucchini et al. 2022; Tramacere et al. 2022). However, the sparsity of our data makes a more detailed study of jet behavior difficult to establish.

Future simultaneous observations from infrared to radio bands are essential to refine our findings and further constrain the jet parameters (e.g., Rodi et al. 2021; Echiburú-Trujillo et al. 2024). Observations at higher radio frequencies above 100 GHz (ALMA) can further constrain the spectral index of the radio spectrum and determine the cooling break of the synchrotron emission (e.g., Russell et al. 2014; Tetarenko et al. 2015), whereas high-sensitivity observations in the infrared (VLT and JWST) can be used to solve the model degeneracy in the synchrotron component of the compact jet region (e.g., Rodi et al. 2021). Additionally, high-sensitivity radio observations below 1 GHz (MeerKAT and SKA) would help determine the transition frequency in the radio band between the optically thin synchrotron emission region and the synchrotron self-absorption region (e.g., Nakar & Piran 2011). These measurements can help constrain the multizone jet parameters and further establish the overall jet structure.

Appendix
MCMC Corner Plots of SED Fitting

In Figure A1, we present the corner plots of the SED fitting parameters from the MCMC for cases (a), (b), and (c) described in Section 3.2.3. These plots show the significant degeneracy between the fitting parameters.
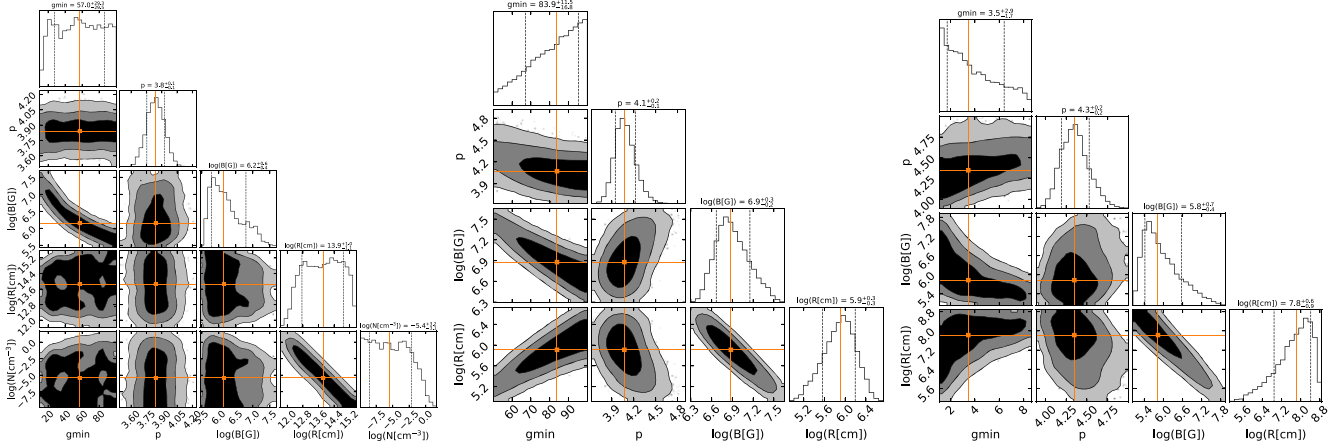

Figure A1. The corner plots of the SED fitting parameters, from left to right, correspond to cases (a), (b), and (c) described in Section 3.2.3. The contours contain the 1, 2, and 3σ confidence intervals, respectively. The central orange line represents the median value of each parameter from the MCMC chain, with two black dashed lines on either side showing the 1σ confidence interval.

ORCID iDs

Zikun Lin ⓘ https://orcid.org/0000-0001-9576-1870
Yanan Wang ⓘ https://orcid.org/0000-0003-3207-5237
Santiago del Palacio ⓘ https://orcid.org/0000-0002-5761-2417
Mariano Méndez ⓘ https://orcid.org/0000-0003-2187-2708
Shuang-Nan Zhang ⓘ https://orcid.org/0000-0001-5586-1017
Thomas D. Russell ⓘ https://orcid.org/0000-0002-7930-2276
Long Ji ⓘ https://orcid.org/0000-0001-9599-7285
Jin Zhang ⓘ https://orcid.org/0000-0003-3554-2996
Liang Zhang ⓘ https://orcid.org/0000-0003-4498-9925
Diego Altamirano ⓘ https://orcid.org/0000-0002-3422-0074

References

Abramowicz, M. A., Czerny, B., Lasota, J. P., & Szuszkiewicz, E. 1988, ApJ, 332, 646
Altamirano, D., Belloni, T., Linares, M., et al. 2011, ApJL, 742, L17
Arnaud, K. A. 1996, in ASP Conf. Ser. 101, Astronomical Data Analysis Software and Systems V, ed. G. H. Jacoby & J. Barnes (San Francisco, CA: ASP), 17
Bachetti, M., Harrison, F. A., Cook, R., et al. 2015, ApJ, 800, 109
Bahramian, A., & Rushton, A. 2022, bersavosh/XRB-LrLx_pub: update 20220908, v220908, Zenodo, doi:10.5281/zenodo.7059313
Ball, D., Sironi, L., & Özel, F. 2018, ApJ, 862, 80
Belloni, T., & Hasinger, G. 1990, A&A, 227, L33
Belloni, T., Klein-Wolt, M., Méndez, M., van der Klis, M., & van Paradijs, J. 2000, A&A, 355, 271
Belloni, T., Méndez, M., King, A. R., van der Klis, M., & van Paradijs, J. 1997, ApJL, 488, L109
Blackburn, J. K. 1995, in ASP Conf. Ser. 77, Astronomical Data Analysis Software and Systems IV, ed. R. A. Shaw, H. E. Payne, & J. J. E. Hayes (San Francisco, CA: ASP), 367
Bosch-Ramon, V., & Khangulyan, D. 2009, IJMPD, 18, 347
Capitanio, F., Giroletti, M., Molina, M., et al. 2009, ApJ, 690, 1621
Chattopadhyay, T., Kumar, A., Rao, A. R., et al. 2024, ApJL, 960, L2
Chaty, S., Dubus, G., & Raichoor, A. 2011, A&A, 529, A3
Corbel, S., Coriat, M., Brocksopp, C., et al. 2013, MNRAS, 428, 2500
Court, J. M. C., Altamirano, D., Pereyra, M., et al. 2017, MNRAS, 468, 4748
Dauser, T., García, J. A., Joyce, A., et al. 2022, MNRAS, 514, 3965
Dauser, T., Wilms, J., Reynolds, C. S., & Brenneman, L. W. 2010, MNRAS, 409, 1534
Done, C., Gierliński, M., & Kubota, A. 2007, A&ARv, 15, 1
Draghis, P. A., Miller, J. M., Costantini, E., et al. 2024, ApJ, 969, 40
Echiburú-Trujillo, C., Tetarenko, A. J., Haggard, D., et al. 2024, ApJ, 962, 116
Eikenberry, S. S., Matthews, K., Morgan, E. H., Remillard, R. A., & Nelson, R. W. 1998, ApJL, 494, L61
Evans, P. A., Beardmore, A. P., Page, K. L., et al. 2007, A&A, 469, 379
Evans, P. A., Beardmore, A. P., Page, K. L., et al. 2009, MNRAS, 397, 1177
Fabian, A. C., Rees, M. J., Stella, L., & White, N. E. 1989, MNRAS, 238, 729
Fender, R. P., Belloni, T. M., & Gallo, E. 2004, MNRAS, 355, 1105
Finke, J. D., Dermer, C. D., & Böttcher, M. 2008, ApJ, 686, 181
Fitzpatrick, E. L. 1999, PASP, 111, 63
Foreman-Mackey, D., Hogg, D. W., Lang, D., & Goodman, J. 2013, PASP, 125, 306
García, F., Karpouzas, K., Méndez, M., et al. 2022, MNRAS, 513, 4196
García, F., Méndez, M., Karpouzas, K., et al. 2021, MNRAS, 501, 3173
García, J., Dauser, T., Lohfink, A., et al. 2014, ApJ, 782, 76
Gatuzz, E., Díaz Trigo, M., Miller-Jones, J. C. A., & Migliari, S. 2020, MNRAS, 491, 4857
Gilfanov, M. 2010, in The Jet Paradigm, ed. T. Belloni, Vol. 794 (Berlin: Springer), 17
Haardt, F., & Maraschi, L. 1993, ApJ, 413, 507
Harvey, M., Rulten, C. B., & Chadwick, P. M. 2022, MNRAS, 512, 1141
Heinz, S. 2004, MNRAS, 355, 835
Hoshino, M. 2013, ApJ, 773, 118
Huppenkothen, D., Bachetti, M., Stevens, A. L., et al. 2019a, ApJ, 881, 39
Huppenkothen, D., Bachetti, M., Stevens, A., et al. 2019b, JOSS, 4, 1393
Illarionov, A. F., & Siuniaev, R. A. 1975, SvA, 18, 413
James, F., & Roos, M. 1975, CoPhC, 10, 343
Janiuk, A., Czerny, B., & Siemiginowska, A. 2000, ApJL, 542, L33
Kaiser, C. R. 2006, MNRAS, 367, 1083
Kantzas, D., Markoff, S., Beuchert, T., et al. 2021, MNRAS, 500, 2112

Kara, E., Steiner, J. F., Fabian, A. C., et al. 2019, Natur, 565, 198
Klein-Wolt, M., Fender, R. P., Pooley, G. G., et al. 2002, MNRAS, 331, 745
Krimm, H. A., Barthelmy, S. D., Baumgartner, W., et al. 2011, ATel, 3144, 1
Krimm, H. A., Holland, S. T., Corbet, R. H. D., et al. 2013, ApJS, 209, 14
Kuulkers, E., Lutovinov, A., Parmar, A., et al. 2003, ATel, 149, 1
Lightman, A. P., Lamb, D. Q., & Rybicki, G. B. 1981, ApJ, 248, 738
Lightman, A. P., & Rybicki, G. B. 1980, ApJ, 236, 928
Liu, Q., Wang, W., Chen, X., et al. 2022, MNRAS, 516, 5579
Lucchini, M., Ceccobello, C., Markoff, S., et al. 2022, MNRAS, 517, 5853
Ma, X., Tao, L., Zhang, S.-N., et al. 2021, NatAs, 5, 94
Makishima, K., Maejima, Y., Mitsuda, K., et al. 1986, ApJ, 308, 635
Markoff, S., Nowak, M. A., & Wilms, J. 2005, ApJ, 635, 1203
Marscher, A. P. 1983, ApJ, 264, 296
Méndez, M., Karpouzas, K., García, F., et al. 2022, NatAs, 6, 577
Méndez, M., Peirano, V., García, F., et al. 2024, MNRAS, 527, 9405
Merloni, A., Heinz, S., & di Matteo, T. 2003, MNRAS, 345, 1057
Merloni, A., & Nayakshin, S. 2006, MNRAS, 372, 728
Miller, J. M., Draghis, P., Gendreau, K., & Arzoumanian, Z. 2022, ATel, 15282, 1
Miller, J. M., Reynolds, M., Kennea, J., King, A. L., & Tomsick, J. 2016, ATel, 8742, 1
Miller-Jones, J. C. A., Tetarenko, A. J., Sivakoff, G. R., et al. 2019, Natur, 569, 374
Mir, M. H., Misra, R., Pahari, M., Iqbal, N., & Ahmad, N. 2016, MNRAS, 457, 2999
Mitsuda, K., Inoue, H., Koyama, K., et al. 1984, PASJ, 36, 741
Miyamoto, S., Kitamoto, S., Mitsuda, K., & Dotani, T. 1988, Natur, 336, 450
Molina, E., del Palacio, S., & Bosch-Ramon, V. 2019, A&A, 629, A129
Motta, S. E., Marelli, M., Pintore, F., et al. 2020, ApJ, 898, 174
Nakar, E., & Piran, T. 2011, Natur, 478, 82
Nathan, E., Ingram, A., Homan, J., et al. 2022, MNRAS, 511, 255
Nayakshin, S., Rappaport, S., & Melia, F. 2000, ApJ, 535, 798
Neilsen, J., Homan, J., Steiner, J. F., et al. 2020, ApJ, 902, 152
Neilsen, J., Remillard, R. A., & Lee, J. C. 2011, ApJ, 737, 69
Neilsen, J., Remillard, R. A., & Lee, J. C. 2012, ApJ, 750, 71
NEOWISE-R Team 2020, NEOWISE-R L1b Images. IPAC, doi:10.26131/IRSA147
Pan, X., Li, S.-L., Cao, X., Miniutti, G., & Gu, M. 2022, ApJL, 928, L18
Planck Collaboration, Aghanim, N., Ashdown, M., et al. 2016, A&A, 596, A109
Punsly, B. 2011, MNRAS, 418, 2736
Pushkarev, A. B., Kovalev, Y. Y., Lister, M. L., & Savolainen, T. 2009, A&A, 507, L33
Pushkarev, A. B., Kovalev, Y. Y., Lister, M. L., & Savolainen, T. 2017, MNRAS, 468, 4992
Remillard, R. A., Loewenstein, M., Steiner, J. F., et al. 2022, AJ, 163, 130
Rodi, J., Tramacere, A., Onori, F., et al. 2021, ApJ, 910, 21
Rodriguez, J., Corbel, S., Caballero, I., et al. 2011, A&A, 533, L4
Rushton, A., Spencer, R., Fender, R., & Pooley, G. 2010, A&A, 524, A29
Russell, D. M., Maitra, D., Dunn, R. J. H., & Markoff, S. 2010, MNRAS, 405, 1759
Russell, D. M., & Shahbaz, T. 2014, MNRAS, 438, 2083
Russell, T., Del Santo, M., D'Aì, A., et al. 2022, ATel, 15286, 1
Russell, T. D., Soria, R., Miller-Jones, J. C. A., et al. 2014, MNRAS, 439, 1390
Russell, T. D., Lucchini, M., Tetarenko, A. J., et al. 2020, MNRAS, 498, 5772
Rybicki, G. B., & Lightman, A. P. 1979, Radiative Processes In Astrophysics (New York: Wiley)
Sari, R., & Esin, A. A. 2001, ApJ, 548, 787
Sari, R., Piran, T., & Narayan, R. 1998, ApJL, 497, L17
Shakura, N. I., & Sunyaev, R. A. 1973, A&A, 24, 337
Shidatsu, M., Ueda, Y., Tazaki, F., et al. 2011, PASJ, 63, S785
Sironi, L., & Spitkovsky, A. 2011, ApJ, 726, 75
Sironi, L., & Spitkovsky, A. 2014, ApJL, 783, L21
Sunyaev, R. A., & Titarchuk, L. G. 1980, A&A, 86, 121
Tetarenko, A. J., Sivakoff, G. R., Miller-Jones, J. C. A., et al. 2015, ApJ, 805, 30
Tetarenko, A. J., Sivakoff, G. R., Miller-Jones, J. C. A., et al. 2017, MNRAS, 469, 3141
Tramacere, A., 2020 JetSeT: Numerical modeling and SED fitting tool for relativistic jets, Astrophysics Source Code Library, ascl:2009.001
Tramacere, A., Giommi, P., Perri, M., Verrecchia, F., & Tosti, G. 2009, A&A, 501, 879
Tramacere, A., Massaro, E., & Taylor, A. M. 2011, ApJ, 739, 66
Tramacere, A., Sliusar, V., Walter, R., Jurysek, J., & Balbo, M. 2022, A&A, 658, A173
van den Eijnden, J., Ingram, A., & Uttley, P. 2016, MNRAS, 458, 3655

Vaughan, S., Edelson, R., Warwick, R. S., & Uttley, P. 2003, MNRAS, 345, 1271

Verner, D. A., Ferland, G. J., Korista, K. T., & Yakovlev, D. G. 1996, ApJ, 465, 487

Vincentelli, F. M., Neilsen, J., Tetarenko, A. J., et al. 2023, Natur, 615, 45

Virtanen, P., Gommers, R., Oliphant, T. E., et al. 2020, NatMe, 17, 261

Wang, J., Mastroserio, G., Kara, E., et al. 2021, ApJL, 910, L3

Wang, J., Kara, E., Lucchini, M., et al. 2022, ApJ, 930, 18

Wang, J., Kara, E., García, J. A., et al. 2024, ApJ, 963, 14

Wang, Y., Méndez, M., Altamirano, D., et al. 2018, MNRAS, 478, 4837

Wilkins, D. R., & Fabian, A. C. 2012, MNRAS, 424, 1284

Wilms, J., Allen, A., & McCray, R. 2000, ApJ, 542, 914

Yan, S.-P., Ji, L., Méndez, M., et al. 2017, MNRAS, 465, 1926

You, B., Cao, X., Yan, Z., et al. 2023, Sci, 381, 961

Zdziarski, A. A. 1985, ApJ, 289, 514

Zdziarski, A. A., Pjanka, P., Sikora, M., & Stawarz, Ł. 2014, MNRAS, 442, 3243

Zdziarski, A. A., Szanecki, M., Poutanen, J., Gierliński, M., & Biernacki, P. 2020, MNRAS, 492, 5234

Zdziarski, A. A., Tetarenko, A. J., & Sikora, M. 2022, ApJ, 925, 189

Zhang, L., Wang, Y., Méndez, M., et al. 2017, ApJ, 845, 143

Zhang, L., Méndez, M., Altamirano, D., et al. 2020, MNRAS, 494, 1375